ASTRONOMY
AND
ASTROPHYSICS

Characteristics of solar coronal streamers

Element abundance, temperature and density from coordinated CDS and UVCS SOHO observations

S. Parenti[1], B.J.I. Bromage[1], G. Poletto[2], G. Noci[3], J.C. Raymond[4], and G.E. Bromage[1]

[1] Centre for Astrophysics, University of Central Lancashire, Preston PR1 2HE, UK
[2] Osservatorio Astrofisico di Arcetri, 50125 Firenze, Italy
[3] Universita' di Firenze, 50125 Firenze, Italy
[4] Harvard-Smithsonian Center for Astrophysics, Cambridge, MA 02138, USA

Abstract. This paper presents the results from coordinated observations of streamers acquired by the SOHO Coronal Diagnostic Spectrometer (CDS) and UltraViolet Coronograph Spectrometer (UVCS) experiments. Data from different altitudes within the solar corona were taken, with the purpose of determining their physical parameters – densities, electron temperatures and element abundances – and their changes over the altitude range between 1.02 and 1.6 $R_\odot$. Further UVCS streamer data, taken about two months later are used for comparison with the behaviour seen in two different streamers. Whenever possible, alternative methods have been adopted to determine the same physical parameter, as a cross check. In particular, the DEM technique has been applied to UVCS data, in order to compare abundance values derived in this way, with those obtained using the method of Raymond et al. (1997). We conclude that abundances in the low corona covered by CDS data do not show evidence for abundance variation, with respect to photospheric values, while, at UVCS altitudes, a depletion of all element abundances is clearly evident. No clear evidence of a FIP effect in streamers was found; we get contrasting results from the only two high FIP elements present in our spectra.

Key words: Sun: abundances – Sun: atmosphere – Sun: corona – Sun: UV radiation

1. Introduction

Coronal streamers are one of the most evident manifestations of solar activity. Visible in white and UV light, they appear as bright, large and long-lived structures that fill the solar corona for several solar radii. White light images show streamers to be shaped like pointed helmets, sometimes arch-like at the base, that taper off and elongate in the interplanetary medium. During solar maximum they can be found at almost every latitude,

---

while during minimum they are located around the solar equator, where most of the activity is concentrated.

Up to a few years ago, most of the information on streamers came from visible continuum eclipse observations from which profiles of density v. height in streamers, imaged at different times during the solar activity cycle, have been evaluated. Following the launch of SOHO in 1995, new information on streamer properties has become available. A "Whole Sun Month" campaign was specifically designed to study the structure of the solar atmosphere at solar minimum, and, as a consequence, descriptions of the 3-D structure of streamers, of their magnetic field, and further density and temperature profiles in streamers have been obtained (Gibson et al. 1999a, 1999b).

However, we would like to draw attention to an unexpected result (Noci et al. 1997), revealed by UVCS, which showed that the hydrogen Lyα (1215 Å) streamer morphology can be quite different from the streamer morphology in O VI lines (at 1032 and 1037 Å): the *maximum* Lyα intensity in the streamer's core may correspond to a *minimum* in O VI line intensities. Raymond et al. (1997) found that the oxygen abundance in the streamer core is typically depleted by a factor ≈ 3, with respect to its coronal value. Further work showed that element abundances can vary from streamer to streamer (Raymond et al. 1998; Li et al. 1998) and even within a streamer (Raymond et al. 1997): along the streamers' edges they resemble the slow wind abundances, thus confirming a scenario where the latter originates in or around streamers. Moreover, Wimmer Schweingruber (1994) has shown that the interface between what was originally slow plasma from the streamer belt and what was fast plasma from coronal holes, is fairly well identified, even at the large heliocentric distances sampled by Ulysses, by variations in composition.

The purpose of the present work is to contribute to a better knowledge of streamer characteristics by evaluating their physical parameters – density, temperature and abundance – from observations taken by two SOHO instruments, CDS (Harrison et al. 1995) and UVCS (Kohl et al. 1995). These observe at different altitudes within the streamer, with CDS data obtained closer to the limb. This kind of analysis has been at-

tempted, so far, only a couple of times: Li et al. (1998) derived the physical parameters of a helmet streamer observed in 1996 from Yohkoh/SXT and SOHO/UVCS data, while Gibson et al. (1999a) compared parameters derived from white light data taken by SOHO/LASCO and HAO/Mark 3 coronographs with densities derived from SOHO/CDS spectra, using the line ratio technique. Our analysis is similar to that of Li et al. (1998), but refers to a slightly different altitude range: Li et al. give values at 1.15 and 1.5 $R_\odot$, while here we present results from ≈ 1.02 to ≈ 1.19 $R_\odot$ from CDS, and at $\approx 1.6R_\odot$, from UVCS data. The capability of deriving physical parameters over a more extended altitude span, at low heights, allows us to make a better estimate of the altitude profiles here. Gibson et al. (1999a), give a more extended density/temperature v. altitude profile (1.1–4 $R_\odot$) than we do here, but do not determine composition.

This work also makes a first attempt at using the Differential Emission Measure (DEM) technique to derive element abundances from UVCS data. The DEM technique has been used in the analysis of spectra acquired by a number of spacecraft (see, e.g., Brosius et al. 1996; Del Zanna & Bromage 1999a; Del Zanna & Bromage 1999b), but UVCS data have never been analyzed with the DEM method, although, as we will see in the following, results from this kind of analysis need to be treated with some caution. A comparison of the DEM results with estimates obtained by alternative techniques, shows the validity of the present evaluation (see Sect. 4.3). The advantage gained by using UVCS data enabled us to reach one of the main conclusions of this paper: including the collisional components of the hydrogen Lyα and Lyβ lines in the DEM curve, the *absolute* values for the element abundances have been determined, rather than values determined relative to oxygen or iron abundances, as is usually the case.

It should be mentioned, however, that the streamers analyzed in this work do not show the same configuration as those analyzed by Raymond et al. (1997), where a weak O VI core corresponds to intense Lyα emission. It has not been ascertained yet, whether there may be two classes of streamers one with and the other without this characteristic. Possibly the stable solar minimum streamers behave differently from active region streamers or the difference may simply be a projection effect.

2. The observations

The work presented here is from two data sets obtained on 8 March 1998 and 7 May 1998. The goal of the March observations was to study the physical characteristics of the streamers at different heliocentric altitudes. To this end, the UVCS and CDS instruments were used to make coordinated observations of two streamers, at different positions along the same radial direction (see Fig. 1). The first streamer was located close to the equator (the "equatorial" streamer) and the second was at a more southerly latitude (the "mid-latitude" streamer).

A similarly located mid-latitude streamer was observed with UVCS in May, for comparison with the March data.
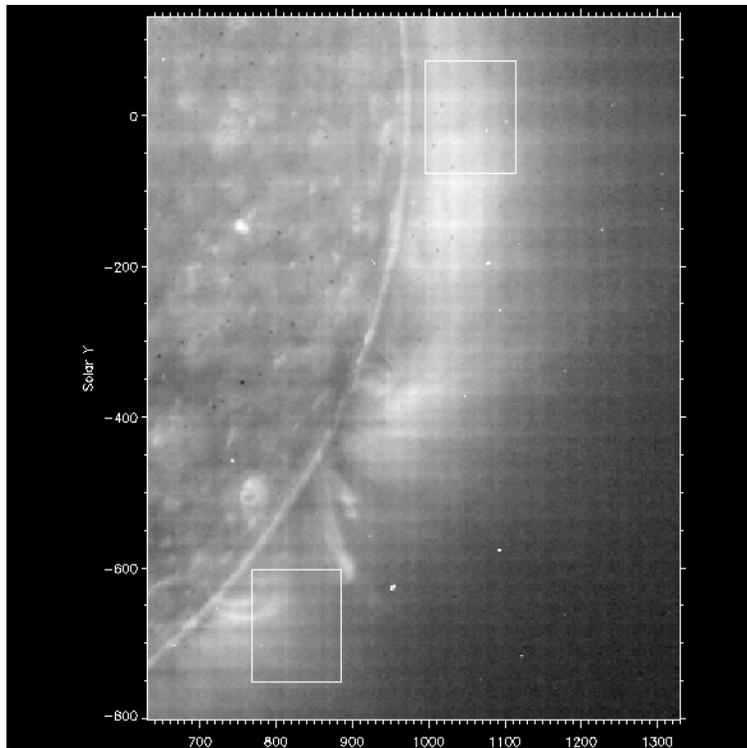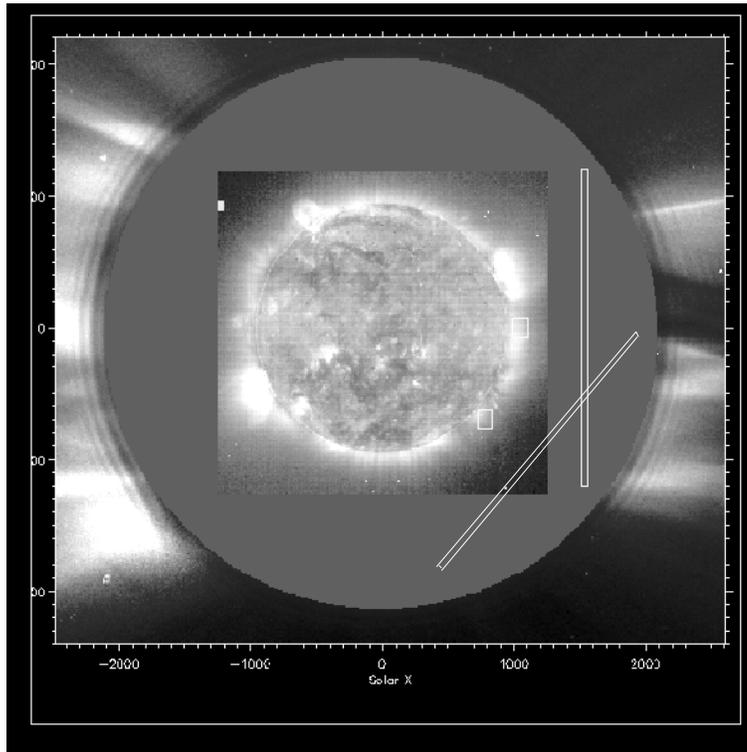
2.1. UVCS observations

UVCS observed the streamers both in the Lyman-alpha and O VI channels with, respectively, a 50 μm and 150 μm wide slits, centred in the South-West quadrant at a heliocentric latitude of: $-0.1°$, for the equatorial observation; $-40°$ for the March mid-latitude data; and $-45°$ for the May observation. In each case, the slit was tangential to the solar limb, at a central distance of $\approx 1.6R_\odot$, its central portion crossing through the brightest Lyα and O VI part of the streamer (see Fig. 2). In the O VI channel, a wide wavelength range was obtained by using three different grating positions, each covering ≈ 100 Å. Individual exposures of 200 s have been integrated over the whole observing time, at each grating position, to increase the statistical significance of the data. The overall integration time was ≈ 5 hours. Data have been taken into the O VI channel with a spatial binning of 10 pixels, giving a spatial resolution of $70''$ ($7''$ for each pixel). The Lyα channel covers a wavelength range of about 50 Å with a spatial resolution of $63''$, given by a spatial binning of 9 pixels ($7''$ for each pixel).

The UVCS data have been calibrated using standard calibration procedures and corrections for flat field effects have been applied (Gardner et al. 1996). Stray light corrections have also been applied, by using UVCS stray light measurements (Gardner, private communication) and disk line intensities from Vernazza & Reeves (1978). The correction have been made using the C III (977 Å) line visible in the oxygen channel, that can be considered completely stray light. This ion, in fact, forms at about $\log T = 4.9$ and it is completely absent in the million Kelvin coronal gas. The streamer spectra we analyzed were obtained by further averaging over the brightest Lyα pixels. For the oxygen channel, the pixels covering the same area were identified and then averaged. Note that the peak of the streamer intensity in O VI corresponded to the peak in the Lyα image.

We note, however, that the March streamer observations were not compensated for cross-talk effects between the telescope mirror mechanism, which determines the pointing, and the grating mechanisms. As a consequence, spectra acquired at different grating positions refer to slightly different heliocentric distances (the difference amounting to no more than 2%). Table 1 lists the spectral lines observed by UVCS which were used in this work.

2.2. CDS observations

CDS data were acquired over a 120×150 arcsec raster, in the South-West quadrant, at a heliocentic latitude of $-0.1°$ for the equatorial streamer, and $-35.35°$ for the mid-latitude streamer, both centred at a heliocentric distance of $1.1R_\odot$. The raster was built up by scanning the slit from west to east over 30 steps. The exposure time at each position was 160 s, and the full wavelength range of the Normal Incidence Spectrometer (NIS) of CDS was used (from 308 to 381 Å and from 513 to 633 Å). The spatial resolution was about $4''$ in both the N-S and the W-E directions. Standard procedures to remove the effects of cosmic rays, together with flat-field, debiasing and geometric correc-

Fig. 1. Composite image of the solar corona from SOHO/EIT and LASCO (top). The CDS rasters and the UVCS slit positions are superimposed on the image. The lower image shows a closer view of the CDS observations, superimposed on the EIT (171 Å) image. A small loop-system can be clearly seen in the top left corner of the mid-latitude raster.

tions were applied using the official CDS software; the spectral lines were fitted using multiple gaussian line-fitting (Haugan 1997) and the intensity calibration from Del Zanna (1999) was applied.

Table 2 shows the lines from the CDS spectra which were used in this study.

2.3. Correspondence between CDS and UVCS March data

Fig. 1 shows an EIT and LASCO composite image of the solar corona on the 8 March, 1998, with the CDS rasters and the UVCS slits superimposed, indicating the location of the observations with respect to the streamers. On the west limb of the
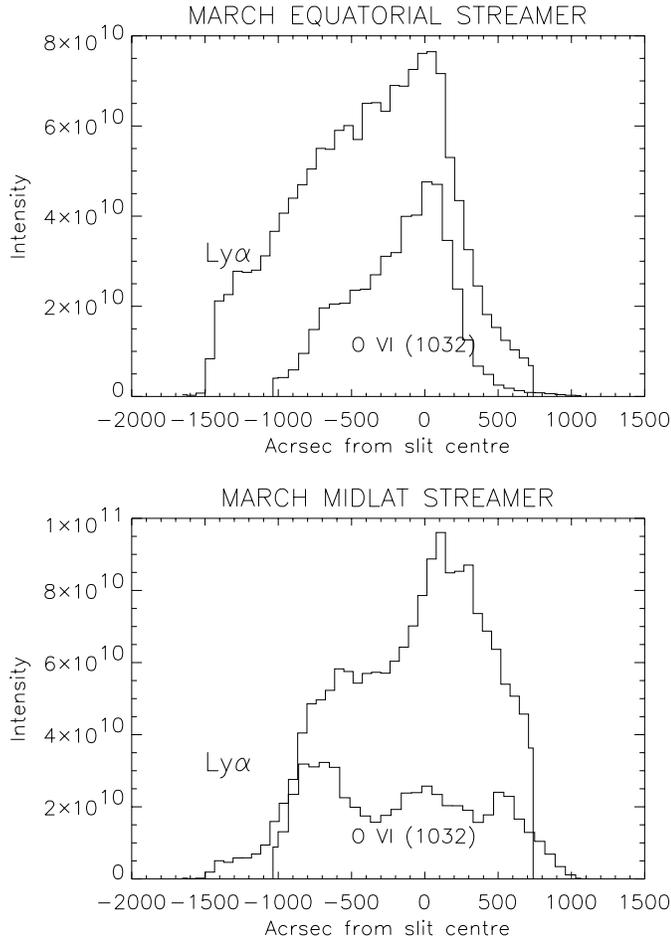
Fig. 2. Profiles of the peak intensities along the UVCS slit for Lyα and O VI (1032) lines, for the equatorial streamer (top) and the mid-latitude streamer (bottom). The intensity scale (*phot cm^{-2} s^{-1} str^{-1} Å^{-1}*) refers to Lyα line.

sun three streamers can be seen, one in the northen hemisphere and two, close together in the southern hemisphere.

Consideration of the images in Fig. 1 along with the profiles in Fig. 2 suggests that the CDS equatorial observation corresponds to the upper edge of the streamers seen by LASCO immediately to the south of the the equator, while the plasma in the mid-latitude CDS observation corresponds to the central part of the lower streamer at that side of the sun. It is worth noting that the range of latitude sampled by CDS is contained within that used for the UVCS analysis and it is much smaller. During the time of the observation, the extended corona sampled by UVCS was largely filled by quiet streamers. Close to the sun, the EIT images showed the CDS raster to be filled by quiet corona at the equator, while a small loop system is seen near the limb in the mid-latitude observation. For the purpose of the abundance determination, a small area external to the loop system was selected and each pixel of this area was summed to obtain an integrated spectrum, representative of the background emission of the streamer. A more detailed study of the hot loop will be discussed in a separate paper.

3. Spectroscopic diagnostics

In the hot plasma of the corona, the dominant processes which form the UV and EUV spectral lines (except Lyα) is collisional excitation from the ground level, with radiative decay being the main process of de-excitation (Mason & Monsignori Fossi 1994). Assuming optically thin radiation, the intensity of a line, can then be expressed as

$$I = \int A_X \, C(T)_{N_e} \, N_e^2 \, \mathrm{d}h \tag{1}$$

where the integral is over the line of sight (h); A_X is the absolute element abundance of the emitting element X and $C(T)_{N_e}$ is the contribution function of the emitting line at the electron density N_e. The CHIANTI database (Dere et al. 1997) has been used to obtain the contribution functions, and the Mazzotta et al. (1998) ioization equilibrium has been adopted.

From Eq. (1) the DEM, as a function of the temperature T can be defined by:

$$DEM(T) = N_e^2 \frac{\mathrm{d}h}{\mathrm{d}T} \tag{2}$$

assuming finite dT, so that the intensity can be rewritten as:

$$I = \int A_X \, C(T)_{N_e} \, DEM(T) \, \mathrm{d}T \tag{3}$$

where the DEM(T) is defined for finite values of $\mathrm{d}h/\mathrm{d}T$. Here, this technique has been applied to the off-limb observations where, more so than on the disc, the variation of temperature along the line of sight is not monotonic.

The DEM(T) is determined in practice by finding the best fit of a discretised spline function to the data. In this way the indeterminate points of the function are avoided. What is obtained in the end, for each interval dT, is a value that best fits the average DEM over the whole line of sight. It should be pointed out that the DEM(T) is a unique function of T but not of h and information of its variation along the line of sight is not obtained. In each element involved there may be a number of lines from different ions. These will give a DEM curve over a limited range of temperature. If another element with lines which overlap the first in temperature is used, the DEM curve for that should align with the first curve. Any shift between the two can be attributed to an error in the adopted abundance of one or the other element. In this way, the abundance of one element relative to the other can be determined and all lines fitted to the one curve. So the determination of the DEM using lines from a number of different elements necessarily results in a determination of the relative abundances of those elements, the only exception being if the lines from a particular element are the only ones in a particular range of temperature. In this case, the best that can be achieved is to ensure that the curve at this point is smoothly connected to the rest of the DEM.

3.1. Collisional and radiative components of the line intensity

For the less dense plasma of the extended corona, another contribution to the total intensity of the line may become important,

Table 1. Line intensities from UVCS (10^{-4} erg/cm²/s/str). $Å_{ID}$ indicates the theoretical wavelength taken from the CHIANTI database.

Line ($Å_{ID}$)	Transition	Equator Mar		Midlat Mar		Midlat May
		$1.58R_\odot$	$1.6R_\odot$	$1.58R_\odot$	$1.6R_\odot$	$1.6R_\odot$
Fe XV 481.450	$3p\ ^1P_1$ - $3p^2\ ^1D_2$	-	-	21.5	-	24.7
Fe XIII] 487.048	$3s^23p^2\ ^3P_1$ - $3s3p^3\ ^5S_2$	5.40	-	16.4	-	-
S XIII 491.463	$2s^2\ ^1S_0$ - $2s.2p^3P_1$	-	-	8.9	-	46.3
Si XII 499.406	$1s^2\ 2s\ ^2S_{1/2}$ - $1s^2\ 2p\ ^2P_{3/2}$	194.6	-	753.3	-	1962.5
Fe XIII] 510.055	$3s^2\ 3p^2\ ^3P_2$ - $3s3p^3\ ^5S_2$	18.3	14.2	-	22.0	10.7
Si XII 520.665	$1s^2\ 2s\ ^2S_{1/2}$ - $1s^22p\ ^2P_{1/2}$	131.9	122.8	505.8	418.3	1148.5
S XII 538.680	$2s^2\ 2p\ ^2P_{3/2}$ - $2s2p^2\ ^4P_{3/2}$	-	-	-	-	17.9
Al XI 550.031	$2s\ ^2S_{1/2}$ - $2p\ ^2P_{3/2}$	-	61.5	-	82.1	180.0
Mg X 624.941	$2s\ ^2S_{1/2}$ - $2p\ ^2P_{1/2}$	-	392.9	-	592.5	1156.4
[Ca XIV] 943.701	$2s^22p^3\ ^4S_{3/2}$ - $2s^22p^3\ ^2D_{3/2}$	-	-	-	-	9.8
[Fe XVIII] 974.858	$2s^22p^5\ ^2P_{3/2}$ - $2s^22p^5\ ^2P_{1/2}$	-	-	-	-	14.2
[Ar XII] 1021.219	$2s^22p^3\ ^4S_{3/2}$ - $2s_22p^3\ ^2D_{5/2}$	4.1	5.7	16.1	10.9	15.0
H I 1025.720		77.2	74.7	71.8	85.9	166.4
[Fe X] 1028.394	$3d\ ^4D_{7/2}$ - $3d\ ^4F_{7/2}$	7.8	6.4	6.5	5.7	6.8
O VI 1031.912	$2s\ ^2S_{1/2}$ - $2p\ ^2P_{3/2}$	827.0	577.6	1441.0	1061.1	2014.7
O VI 1037.614	$2s\ ^2S_{1/2}$ - $2p\ ^2P_{1/2}$	293.8	194.6	570.6	410.3	748.0
[S X] 1196.244	$2p^3\ ^4S_{3/2}$ - $2p^3\ ^2D_{5/2}$	-	-	-	-	34.7
H I 1215.740		26058.2	23452.4	23126.7	20683.7	27198.2
[Fe XII] 1242.005	$3p^3\ ^4S_{3/2}$ - $3p^3\ ^2P_{3/2}$	54.3	31.2	21.7	15.9	16.1

that is the radiative excitation due to the resonantly scattered light coming from the lower solar atmosphere (Gabriel et al. 1977; Withbroe et al. 1982). In these data, only H-Lyman and O VI lines from UVCS can be considered affected by radiative excitation, and for the purpose of this study the two contributions have been separated.

The radiative (*Rad*) and collisional (*Col*) component of the Lyβ line together with those of Lyα, were derived by using the observed intensities of the Lyα and the Lyβ lines and the predicted ratios between their radiative ($Rad_{Ly\alpha}/Rad_{Ly\beta}$) and collisional components ($Col_{Ly\alpha}/Col_{Ly\beta}$). Mazzotta et al. do not give the ionization balance for H. We computed the hydrogen neutral fraction using the ionization rate of Scholz & Walters (1991) and recombination rates from Hummer (1994). The contribution of recombination to excited levels from Hummer & Storey (1987) was added to the Lyman line excitation rates of Callaway (1994). The ratio between Lyα and Lyβ radiative components is independent of electron temperature, while the ratio of their collisional components is nearly independent of temperature at coronal temperatures.

The two components of the O VI at 1032 and 1037 Å lines have been derived from the simple relationships between the intensities of the collisionally excited and radiatively excited components of the doublet (Noci et al. 1987):

$$\frac{I_{col}(1032)}{I_{col}(1037)} = 2 \tag{4}$$

$$\frac{I_{rad}(1032)}{I_{rad}(1037)} = 4 \tag{5}$$

and the total intensity of the doublet lines I is given by $I = I_{tot} = I_{rad} + I_{col}$.

3.2. Temperature diagnostics

The simplest method used to determine temperature was the line ratio technique. From Eq. (1), assuming isothermal plasma, it can be seen that the ratio of lines from the same element, in close stages of ionization, is a function of temperature only – if a constant density is assumed along the line of sight and if ionization equilibrium holds. This technique was applied to data from both CDS and UVCS, on the grounds that the streamer plasma should be static (at least at the low altitudes we are dealing with in this work) and that for UVCS most of the emission should come from the high density plasma close to the streamer's axis with negligible contribution from the surrounding low density atmosphere.

The best element to be used in the line ratio technique turned out to be Fe because it is present in both the UVCS and CDS spectra, in bright and well-defined lines from different stages of ionization. For CDS data diagnostics, the ratios Fe XII (364.467 Å)/ Fe XI (352.662 Å), Fe XI (352.662 Å)/Fe X (345.723) and Fe XIII (348. Å)/ Fe X (345.7 Å) have been used. The last ratio allows a direct comparison with UVCS because the Fe XIII (510 Å) and Fe X (1028 Å) lines are the brightest Fe lines in the UVCS spectra. Moreover, the chosen lines, at a given temperature T, have a constant ratio over the range of density encountered here ($10^6 < N_e < 10^9$ cm^{-3}). Electron temperatures have been calculated using Mazzotta et al. (1998) ionization equilibria.

A slightly different way to estimate the electron temperature from UVCS data, deriving at the same time the element abundance, has been developed by Raymond et al. (1998). In this technique, the ratio R of the predicted emissivity to the observed intensity of an ion (calculated with photospheric abundance (Feldman 1992)), relative to the same ratio for the hydrogen Lyβ collisional component (see equation below) is plotted

Table 2. Line intensities from CDS (erg/cm^2/s/str). Å$_{ID}$ indicates the theoretical wavelenght taken from the CHIANTI database.

Line (Å)	Transition	Equator 1.1 $R_\odot$	Midlat 1.1 $R_\odot$
Mg VIII 313.754	2p ^{2}P$_{1/2}$ - 2s 2p^2 ^{2}P$_{1/2}$	4.4	3.5
Mg VIII 315.039	2p ^{2}P$_{3/2}$ - 2s.2p^2 ^{2}P$_{3/2}$	9.4	10.5
Si VIII 316.205	2s^{2}2p^3^{4}S$_{3/2}$ - 2s2p^4 ^{4}P$_{3/2}$	11.6	19.3
Mg VIII 317.039	2p ^{2}P$_{3/2}$ - 2s.2p^2 ^{2}P$_{1/2}$	3.6	-
Si VIII 319.826	2s^{2}2p^3 ^{4}S$_{3/2}$ - 2s2p^4 ^{4}P$_{5/2}$	19.5	-
Fe XIII 321.400	3s^2 3p^2 ^{3}P$_2$ - 3s 3p^3 ^{3}P$_1$	3.1	32.2
Fe XV 327.011	3s3p ^{3}P$_2$ - 3p^2 ^{1}D$_2$	-	24.3
Al X 332.789	2s^2 ^{1}S$_0$ - 2s2p ^{1}P$_1$	15.6	59.9
Fe XIV 334.172	3s^2 3p ^{2}P$_{1/2}$ - 3s 3p^2 ^{2}D$_{3/2}$	13.6	358.7
Mg VIII 339.006	2p ^{2}P$_{3/2}$ - 2s2p^2 ^{2}S$_{1/2}$	2.6	2.9
Fe XI 341.113	3s^{2}3p^4 ^{3}P$_2$ - 3s3p^5 ^{3}P$_1$	7.9	16.9
Fe X 345.723	3s^{2}3p^5 ^{2}P$_{3/2}$ - 3s3p^6 ^{2}S$_{1/2}$	9.8	9.7
Fe XII 346.852	3s^{2}3p^3 ^{4}S$_{3/2}$ - 3s3p^4 ^{4}P$_{1/2}$	11.6	41.5
Si X 347.403	2p ^{2}P$_{1/2}$ - 2s2p^2 ^{2}D$_{3/2}$	44.6	-
Fe XIII 348.183	3s^2 3p^2 ^{3}P$_0$ - 3s 3p^3 ^{3}D$_1$	16.6	110.8
Fe XII 352.106	3s^{2}3p^3 ^{4}S$_{3/2}$ - 3s3p^4 ^{4}P$_{3/2}$	-	68.2
Fe XI 352.662	3s^{2}3p^4 ^{3}P$_2$ - 3s3p^5 ^{3}P$_2$	23.5	44.5
Fe XVI 360.8	3s ^{2}S$_{1/2}$ - 3p ^{2}P$_{1/2}$	2.0	434.3
Fe XII 364.467	3s^{2}3p^3 ^{4}S$_{3/2}$ - 3s.3p^4 ^{4}P$_{5/2}$	31.5	113.2
Mg IX 368.070	2s^2 ^{1}S$_0$ - 2s.2p ^{1}P$_1$	88.7	137.1
Fe XI 369.153	3s^{2}3p^4 ^{3}P$_1$ - 3s3p^5 ^{3}P$_2$	6.0	10.4
Si XII 520.665	1s^{2}2s ^{2}S$_{1/2}$ - 1s^{2}2p ^{2}P$_{1/2}$	4.6	107.4
Al XI 550.031	1s^2(1s)2s ^{2}S$_{1/2}$ - 1s^2(1s)2p ^{2}P$_{3/2}$	3.1	24.7
O IV 554.513	2s^{2}2p ^{2}P$_{3/2}$ - 2s2p^2 ^{2}P$_{3/2}$	0.2	0.4
Ca X 557.765	3s ^{2}S$_{1/2}$ - 3p ^{2}P$_{3/2}$	2.9	10.4
Ne VII 561.728	2s2p ^{3}P$_2$ - 2p^2 ^{3}P$_2$	0.1	-
Ne VII 561.4	2s2p ^{3}P$_1$ - 2p^2 ^{3}P$_1$		
Ne VI 562.803	2s^2 2p ^{2}P$_{3/2}$ - 2s 2p^2 ^{2}D$_{5/2}$	0.1	0.5
Al XI 568.120	1s^2(1s).2s ^{2}S$_{1/2}$ - 1s^2(1s).2p ^{2}P$_{1/2}$	1.5	-
Ca X 574.010	3s ^{2}S$_{1/2}$ - 3p ^{2}P$_{1/2}$	-	5.7
O III 599.597	2s^{2}2p^2 ^{1}D$_2$ - 2s2p^3 ^{1}D$_2$	-	0.3
Mg X 609.793	1s^2(1s).2s ^{2}S$_{1/2}$ - 1s^2(1s).2p ^{2}P$_{3/2}$	43.9	160.7
Si X 621.079	2p ^{2}P$_{1/2}$ - 2s.2p^2^{4}P$_{1/2}$	-	1.6
Mg X 624.941	1s^2(1s)2s ^{2}S$_{1/2}$ - 1s^2(1s)2p ^{2}P$_{1/2}$	19.5	75.9
O V 629.730	2s^2 ^{1}S$_0$ - 2s.2p ^{1}P$_1$	0.4	0.6

as a function of temperature. By using ions of the same element and determining the temperature at which the log R v. log T curves of the individual ions intersect, the plasma electron temperature can be identified. A common intersection is found whenever the plasma is strictly isothermal (within the uncertainties in atomic rates and instrumental radiometric calibration).

$$R_{th} = \frac{[A_X \cdot C(T)]_{ion}}{[A_X \cdot C(T)]_{Ly\beta,c}}; \qquad R_{obs} = \frac{I_{ion}}{I_{Ly\beta,c}}; \qquad (6)$$

$$R = R_{th}/R_{obs} \qquad (7)$$

where I_{ion} is the observed ion intensity and $I_{Ly\beta,c}$ is the collisional component of the H-Lyman beta line. As a reference ion we adopted iron, because it is present in a number of ionization stages in the spectra and the results from this technique can be compared with those from the line ratio technique.

An analogous set of curves can be produced for the CDS data. However, because of the absence of the H lines in CDS spectra, the ratio $C(T)_{Fe}/I_{Fe}$ of the contribution function of the iron ion to the observed intensity must be used to look at the plasma temperature distribution.

The third method of determining the temperature was from the DEM. This shows the temperature at which the peak(s) in emission occur(s) (see e.g. Fig. 8).

3.3. Density diagnostic

The average density along the line of sight, in the CDS data, has been estimated by applying the line ratio technique. This consists of calculating the density-dependent ratio of two lines of the same ion in order to obtain a quantity dependent only on the density of the emitting plasma. A line can be density-sensitive in a certain density range, when one transition involves a metastable level whose collisional depopulation strength is comparable to the spontaneous emission (Mason & Monsignori Fossi 1994). Good diagnostic ratios in CDS spectra are provided by the Si X 356/347.4 Å line ratio and by the Si IX 349.9/341.9 Å line ratio. These ratios are density-dependent for $10^6 < N_e <$

10^9 cm^{-3}. The coronal densities are expected to fall within this range.

No density-sensitive lines are present in UVCS spectra; hence we made an estimate of densities from the ratio of the radiative and collisional components of the O VI 1032 Å line. For a nearly static plasma, as we expect in a streamer at 1.6 $R_\odot$, Doppler dimming is negligible and the technique suggested by Noci et al. (1987) can be applied. They show that the ratio of radiative to collisional intensities of O VI is given by:

$$\frac{I_{\rm rad}}{I_{\rm col}} = 5.75 \times 10^2 \frac{\lambda^2 \exp[E/kT]\sqrt{T} \int I_{\rm disk}(\lambda)d\lambda}{\overline{g}N_{\rm e}(\Delta\lambda_{\rm cor}^2 + \Delta\lambda_{\rm ex}^2)^{1/2}} \quad (8)$$

$$\times \left(\frac{R_\odot}{r}\right)^2 Q(r)$$

where $\lambda = 1031.912$ Å; E is the energy difference between the levels involved in the transition (1.9251×10^{-11} erg); T is the electron temperature; $I_{\rm disk}$ is the line intensity integrated over the disk (305 ergs cm^{-2} s^{-1} sr^{-1}, Vernazza & Reeves 1978); $\overline{g}$ is the effective Gaunt factor (1.13); $\Delta\lambda_{\rm ex}$ is the e^{-1} half-width of the exciting line from the lower atmosphere (0.10 Å); $\Delta\lambda_{\rm cor}$ is the e^{-1} half-width of the coronal absorption profile (0.11 Å); $Q(r) = 2[1 - (1 - R_\odot^2/r^2)^{0.5}]r^2/R_\odot^2$ is the solid angle subtended by the solar disk at a distance r and $N_{\rm e}$ is the electron density. Values of $I_{\rm rad}/I_{\rm col}$ have been derived from our data; for T we adopted values from the line ratio technique (see Sect. 4.1) and we refer the reader to the Noci et al. (1987) paper for all the other quantities.

3.4. Determining element abundances

For the UVCS data, absolute abundance can be obtained from the log R v. log T curve described above in Sect. 3.2, from the vertical offset from zero, where the curves cross. UVCS data also allow us to derive the *absolute* abundance of oxygen using O VI 1032 Å. Once the collisional and radiative contributions of the O VI 1032 and Lyβ lines are known, we may write (see Raymond et al. 1997):

$$\left(\frac{N_{\rm O}}{N_{\rm H}}\right)_{\rm rad}$$
$$= \frac{I_{\rm rad}(1032)}{I_{\rm rad}(L\beta)} \frac{C_{\rm HI}}{C_{\rm OVI}} \frac{B_{\rm L\beta}}{B_{\rm OVI}} \frac{f_{\rm L\beta}}{f_{1032}} \frac{I_{\rm disk}(L\beta)}{I_{\rm disk}(1032)} \frac{\delta\nu_{\rm OVI}}{\delta\nu_{\rm HI}} \quad (9)$$

and:

$$\left(\frac{N_{\rm O}}{N_{\rm H}}\right)_{\rm col} = \frac{I_{\rm col}(1032)}{I_{\rm col}(L\beta)} \frac{C_{\rm HI}}{C_{\rm OVI}} \frac{B_{\rm L\beta}}{B_{\rm OVI}} \frac{q_{\rm L\beta}}{q_{1032}} \quad (10)$$

where $(N_{\rm O}/N_{\rm H})_{\rm col}$ and $(N_{\rm O}/N_{\rm H})_{\rm rad}$ indicate the oxygen abundance value derived from the collisional and radiative components of the line intensity; $I_{\rm col}$ and $I_{\rm rad}$ are the collisional and radiative components of the intensity in phot/cm^2/s/str; $C_{\rm OVI}/C_{\rm HI}$ is the ratio of ion concentration (which, in the log T interval 6.1-6.3 changes by $\leq 16\%$); f is the oscillator strength; B is the branching ratio; $I_{\rm disk}$ is the disk intensity in O VI/Lyβ lines; $\delta\nu$ is the line width and q the excitation rate. We refer to Raymond et al. (1997) for the values used for these parameters. The results from this analysis are presented in Sect. 4.3.

The DEM technique has been used to derive the element abundances for both UVCS and CDS data. Moreover, it allows also to compare oxygen abundance values derived from UVCS data using two different techniques (Withbroe 1978). The DEM technique requires lines to be collisionally excited, hence, in the following, we use the collisional components of the O VI and neutral hydrogen lines in the UVCS data, and assume all other lines, listed in Table 1, to have no radiative component. This is certainly the case for lines which form at such high temperatures that their disk emission may be considered negligible. For the CDS data, as already mentioned, the lines can be considered to be formed collisionally.

4. Results and discussion

4.1. Temperatures

From CDS data we have been able to derive the profile of temperature v. heliocentric distance, over the range 1.02–1.19 $R_\odot$, both for the March equatorial and the March mid-latitude streamers, from spectra obtained by dividing the rasters into concentric slices, $10''$ wide for the equatorial and $15''$ wide for the mid-latitude case. The profile for the equatorial data is given in Fig. 3 (top panel) and the profile for the mid-latitude streamer appears in the bottom panel of the same figure. The temperature increases with distance, from the limb up to the maximum distance covered by our spectra, in both profiles. Although CDS spectra have been taken low in the corona, where coronal activity may well affect the data and show up as a multithermal plasma, temperatures from different ion ratios are very similar, suggesting, at each altitude, a quasi-isothermal plasma. Moreover, the equatorial data seems to converge to isothermal at $1.1R_\odot$ from the sun centre.

However, we cannot rule out the possibility that the temperatures of the mid-latitude streamer, higher than those of the equatorial streamer, are due to a "contamination" of the area we chose as representative of the streamer emission, by the hot loop present in the CDS field of view.

The data points at 1.58 $R_\odot$ and 1.6 $R_\odot$ on the same figures represent the temperatures derived from UVCS spectra taken at different grating positions that, for the March observations, correspond to different solar distances. At $1.58R_\odot$ temperatures obtained from the Fe XIII/ Fe X line ratio are 1.28 $\pm$ 0.02 $\times$ 10^6 K for the mid-latitude and 1.24 $\pm$ 0.01 $\times$ 10^6 K for the equatorial streamer; at 1.6 $R_\odot$ temperatures are 1.28 $\pm$ 0.02 $\times$ 10^6 K at mid-latitude and 1.23 $\pm$ 0.01 $\times$ 10^6 at the equator. These values are consistent with CDS temperatures, provided we assume streamer coronal temperatures to first increase with altitude and, after reaching a maximum beyond ≈ 1.25 $R_\odot$, to slowly decrease. This behaviour is to be expected, if the streamer plasma is approximately in thermal equilibrium and the scale-height temperature does not differ significantly from the electron temperature. Gibson et al. (1999a) scale-height temperatures, for instance, peak at $\approx 1.3 - 1.4$ $R_\odot$ and, at 1.6 $R_\odot$, are in the
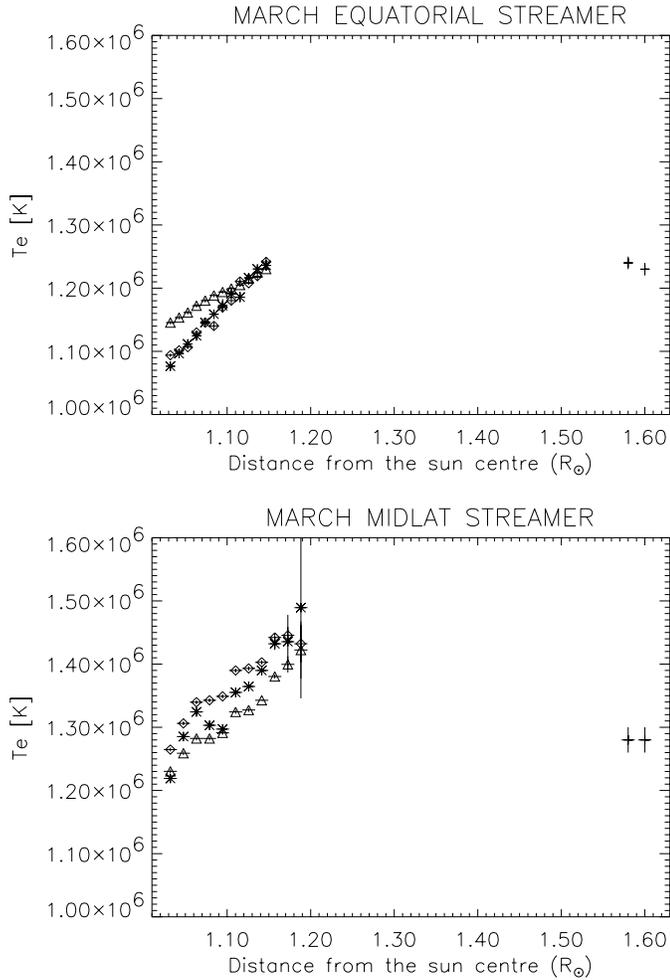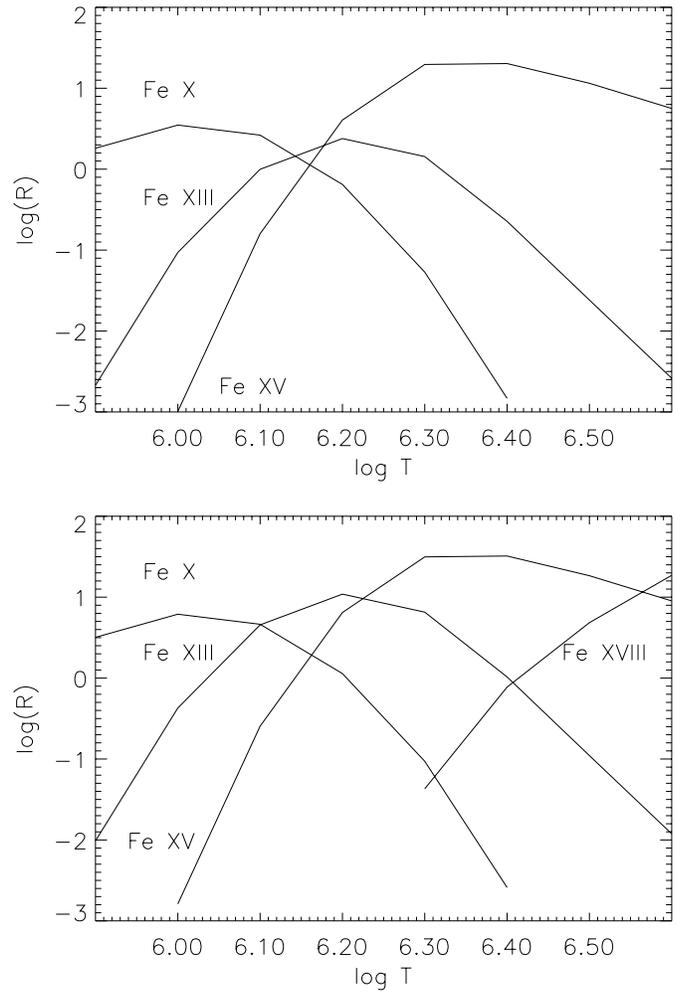
Fig. 3. Temperature *v.* distance from the Sun centre for the March equatorial (top panel) and midlatitude (bottom panel) streamers. The triangles are the temperatures from CDS Fe XIII 348.183/ Fe X 345.723; asterisks are the temperature from CDS Fe XI 352.662/ Fe X 345.723; diamonds are the temperatures from CDS Fe XII 364.467/ Fe XI 352.662; crosses are the temperatures from UVCS Fe XIII 510/ Fe X 1028. Error bars represent statistical errors.

Fig. 4. $\log R$ v. $\log T$ for the March mid-latitude data at 1.58 R$_\odot$ (top panel) and May mid-latitude data at 1.6 R$_\odot$ (bottom panel).

range $1.3 - 1.55 \times 10^6$ K, in good agreement with the present results.

Fig. 4 gives (top panel) the $\log R$ v. $\log T$ curves (see Eq. (7)) for the mid-latitude streamer, from Fe X, Fe XIII and Fe XV lines, at $1.58 R_\odot$ (spectra taken at 1.6 $R_\odot$ contain too few iron ions to be used for this estimate). The temperature, given by the average value at the intersection of these curves, is found to be $1.4 \pm 0.2 \times 10^6$ K. The equatorial spectra did not contain enough iron lines for this technique to be applied.

March mid-latitude temperature values agree fairly well with values derived from line ratios, being $\leq 10\%$ higher. However, in the May spectra, hot ions like Fe XVIII (974.858 Å line), appear to coexist with the cooler ions (Fe X), indicating a multithermal plasma. This is confirmed by the bottom panel of Fig. 4, where the $\log R$ v. $\log T$ curves for different ions intersect over a wide range of temperature.

We mention here that lines from Fe XII have not been used in Fig. 4, because they seem to be inconsistent with other Fe lines. This also affect the DEM analysis (see Sect. 4.3).

The DEM analysis gives temperatures in agreement with those found by the other two methods. For the March streamers, the data points on the DEM plots (Fig. 7) are localized in a narrow range of temperatures between $\log T = 6$ and $\log T = 6.15$, with no lines originating at higher/lower temperatures. This indicates a nearly isothermal streamer plasma at a temperature between 1 and 1.4×10^6 K, while in the May streamer, the data points spread over a wider range of temperatures ($6 < \log T < 6.65$) and an assumption of an isothermal streamer is clearly not justified. This agrees very well with the results obtained from the $\log T$, $\log R$ curves described above.

Fig. 5 gives the $\log(C(T)_{Fe}/I_{Fe})$ v. $\log T$ curves for the CDS data. The observed lines of the iron ions are taken from Table 2. For the midlatitude data (top panel) the intersection points of the different curves lie in the temperature interval $6.15 < \log T < 6.35$, that corresponds to the region of maximum emission derived from the DEM analysis (see Fig. 8). The same was true for the equatorial data (bottom panel), and the interval of tem-
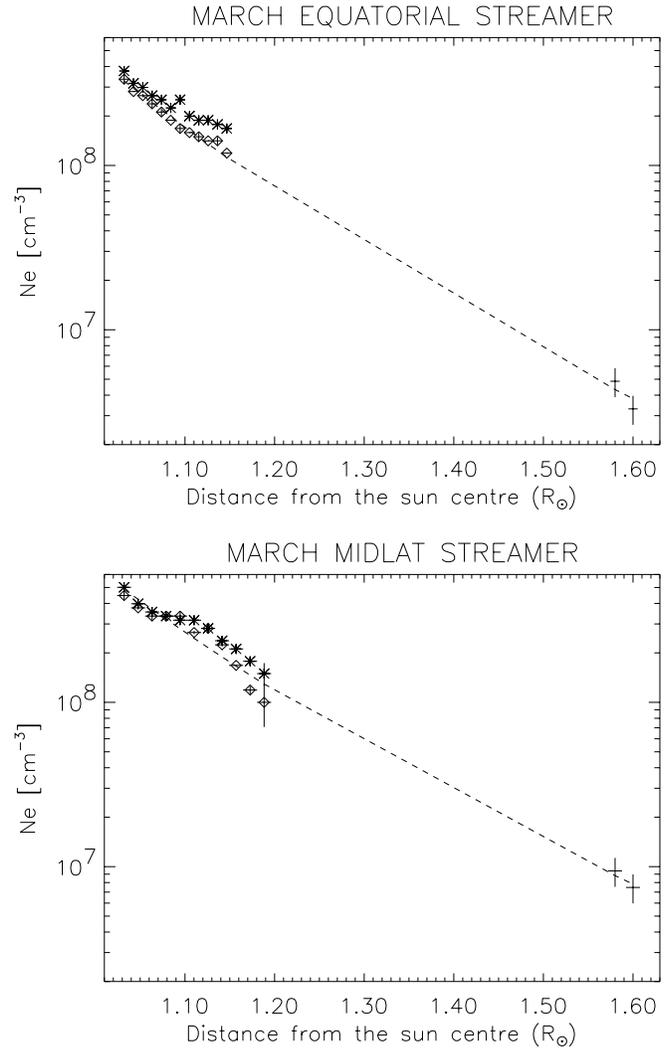
MARCH EQUATORIAL STREAMER

MARCH MIDLAT STREAMER
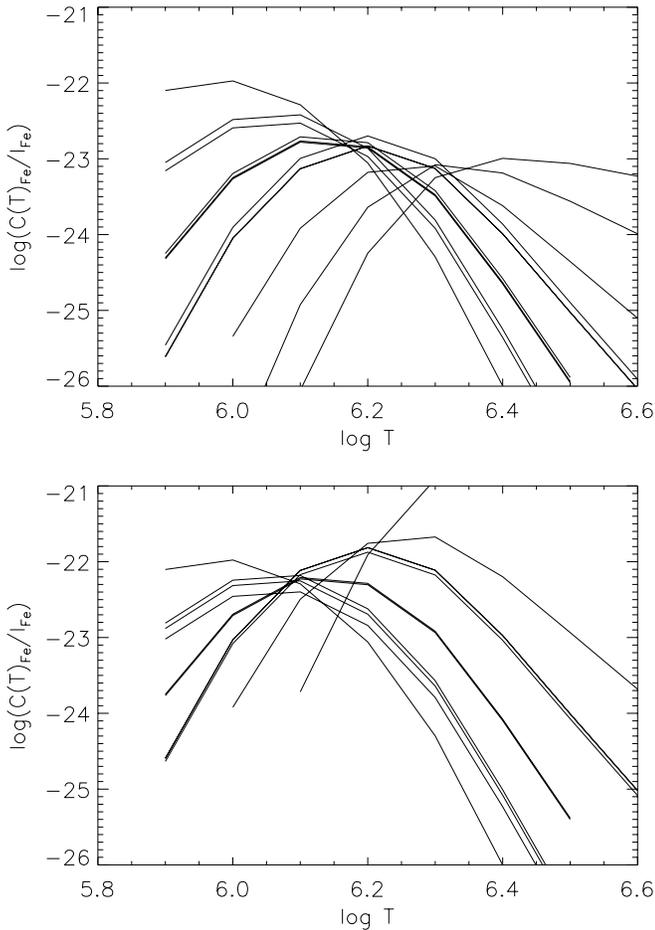
Fig. 5. $\log{(C(T)_{\rm Fe}/{\rm I}_{\rm Fe})}$ v. $\log T$ for the March mid-latitude (top panel) and equatorial data (bottom panel) at 1.1 R$_\odot$.

Fig. 6. Density profile *v.* distance from the Sun centre. The diamonds represent the density from CDS Si IX 349.9/341.9, the asterisks the density from CDS Si X 356/347 and the triangles the density from UVCS. The dashed lines represent the least-square fits (see text), to the density from CDS Si IX and UVCS (O VI resonance doublet) data. Top panel: March equatorial data; Bottom: March midlatitude data.

peratures given by the iron lines is limited to $6.1 < \log T < 6.2$. This is a clear indication of cooler and more isothermal plasma than that shown at midlatitude.

4.2. Densities

Profiles of density v. heliocentric distance have been derived from the March CDS data, using spectra averaged over the concentric slices obtained from the raster (see Sect. 4.1). Densities derived from both Si IX and Si X line ratios have been plotted *v.* solar distance for the equatorial and mid-latitude data in Fig. 6. Densities from the two ratios are in good agreement: in both streamers the density decreases with distance, but at any distance it is higher for the mid-latitude structure. In this, a signature of the loop present in the CDS field of view appears at about 1.09 R$_\odot$, with the density remaining almost constant over a distance of about 30″. The fall in density then resumes.

In the same figure, densities derived from March UVCS data using Eq. (8) have been plotted. The complete sets of densities derived from UVCS data are summarized in Table 3. UVCS results give higher densities at mid-latitude than at the equator: this is consistent with CDS results. A linear least squares fit to the log-log variation of density with distance (using CDS Si IX

Table 3. Density and temperatures from UVCS data. The temperatures are in 10^6 K units and densities in cm^{-3}

Region	$I_{1032,\rm rad}/I_{1032,\rm col}$	T	$N_{\rm e}$
Equator Mar 1.58 R$_\odot$	1.33	1.24	4.86×10^6
Equator Mar 1.6 R$_\odot$	1.81	1.23	3.30×10^6
Midlat Mar 1.58 R$_\odot$	0.69	1.28	9.42×10^6
Midlat Mar 1.6 R$_\odot$	0.80	1.28	7.47×10^6
Midlat May 1.6 R$_\odot$	1.00	1.26	6.08×10^6

and UVCS data), give indices for the power law variation of -10.1 for the equatorial data and -9.42 for the mid-latitude data. These fits have been superimposed on the plots in Fig. 6, allowing for the now linear distance scale. If the initial density from this ion, and the temperature (e.g. Fe XIII/X) from
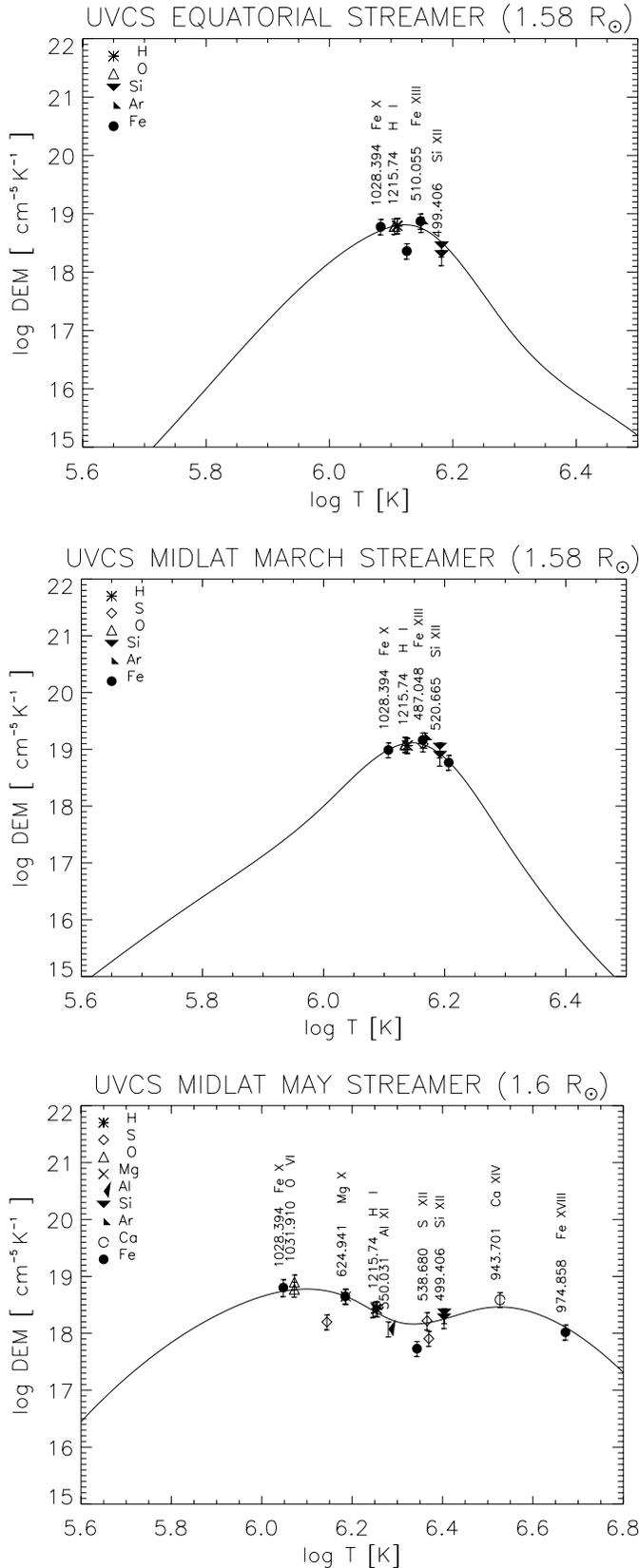
Fig. 7. log DEM v. log T for UVCS data. Top panel: equatorial streamer; middle panel: mid-latitude streamer for March data; bottom panel: mid-latitude streamer for May data. The DEMs are relative to hydrogen, which abundance is taken from Table 5.

Table 4. Absolute O abundance for the UVCS data, in "dex". The values presented here in column 3 are the average of those obtained separately from the radiative (column 2) and collisional (column 1) components of O VI (1032) and Lyβ lines. Note that the photospheric abundance of O is 8.93.

Region	O/H (Col)	O/H (Rad)	O/H (Aver.)
Equator Mar 1.58 $R_\odot$	8.15	8.42	8.29
Equator Mar 1.6 $R_\odot$	7.91	8.36	8.14
Midlat Mar 1.58 $R_\odot$	8.32	8.57	8.44
Midlat Mar 1.6 $R_\odot$	8.24	8.52	8.38
Midlat May 1.6 $R_\odot$	8.12	8.74	8.43

CDS are taken, and hydrostatic equilibrium is assumed, values of density of 1.6×10^7 and 6.7×10^6 cm^{-3} are predicted at 1.6 $R_\odot$ for, respectively, the mid-latitude and equatorial streamers. These values, close to the UVCS results, confirm that the decreasing density with heliocentric distance, over the CDS and UVCS altitude range can be reproduced by assuming hydrostatic equilibrium (e.g. Gibson et al. 1999a, see discussion in Sect. 5).

4.3. Element abundance

Iron abundances were derived from the average value of the offset from 0 of log R at the intersection of the log R v. log T curves of Fig. 4 (see Eq. (7)). This technique gives the offset as a function of the ratio of the abundance of Fe to that of H. The abundance determined by this method is therefore an *absolute* value. The Fe abundance was found to be slightly less than photospheric in the March mid-latitude streamer, but it was 50% lower than the photospheric abundance in the May streamer (see Table 5).

Values of the oxygen abundance for the March and May streamers are presented in Table 4. They are calculated from the average of the "collisional" and "radiative" estimates obtained from Eq. (9) and Eq. (10). As Raymond et al. (1997) found, abundances from the collisional component appear to be systematically lower than abundances from the radiative component. They suggested that this was either because of a physical difference in the abundances of higher density regions (heavily weighted by the collisional contribution, which depends on the square of the density), or because of a small error in the separation of the collisional and radiative components of the Lyβ line. We notice also that abundances derived from Eq. (8) strongly depend on the values assumed for the Lyβ and O VI (1032) disk intensities. Noci and Maccari (private communication), for instance, derive a different value (about 30% higher) for the ratio of the radiative components of the H Lyα and Lyβ lines than Raymond et al. (1997) found, mostly because of a different choice for the values of disk intensities. In absence of disk measurements simultaneous to our coronal data, we adopted Raymond at al. values, but it may well be that the discrepancy in our calculations of abundances from radiative and collisional components has to be ascribed to an inaccurate knowledge of disk intensities at the time of our streamer data.

CDS EQUATORIAL STREAMER (1.1 R$_\odot$)

CDS MIDLAT STREAMER (1.1 R$_\odot$)
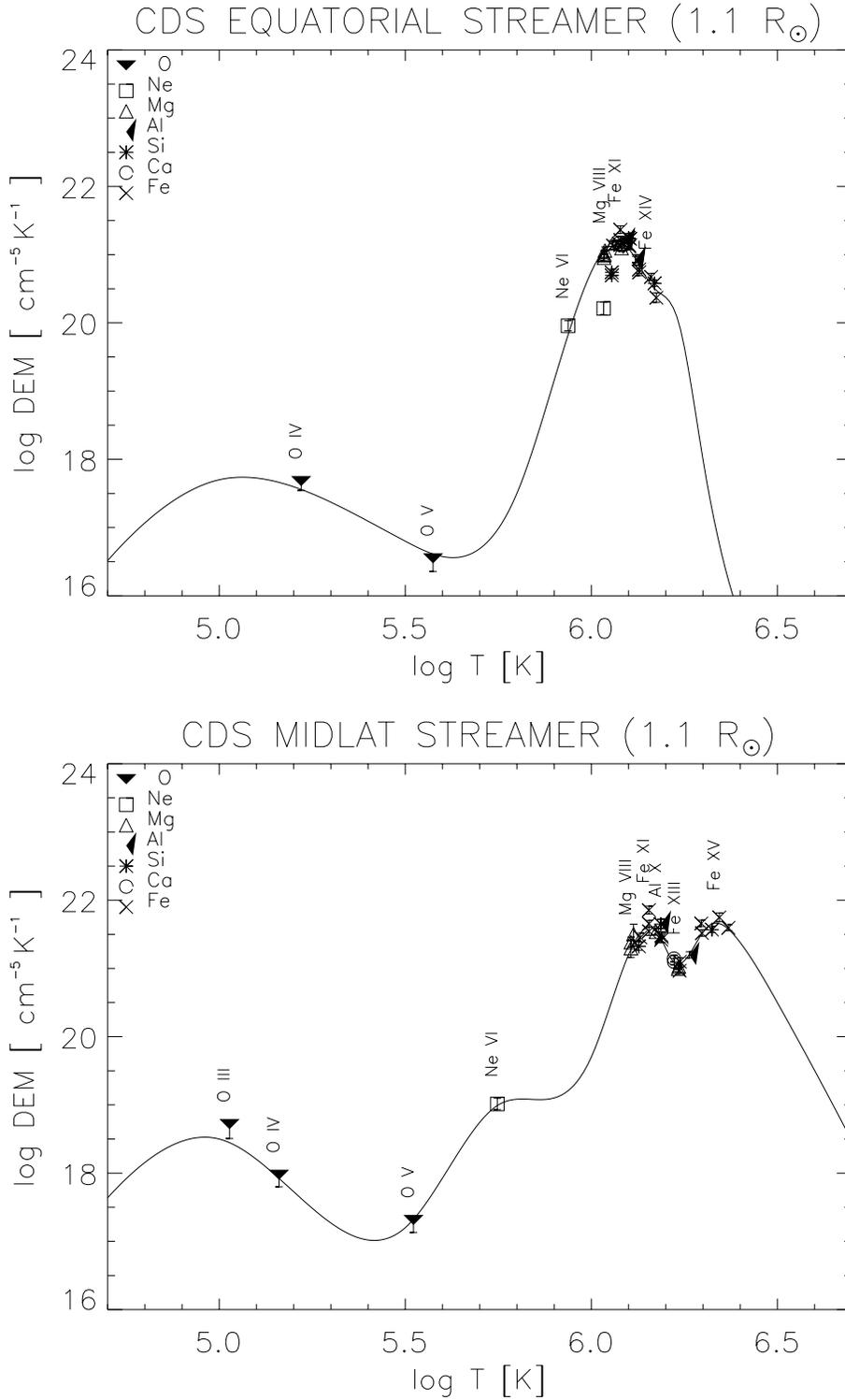
Fig. 8. log DEM v. log T for CDS data. Top panel: equatorial streamer; bottom panel: mid-latitude streamer. The DEMs are relative to photospheric iron; O and Ne abundances are assumed photospheric.

The results clearly show a depletion of oxygen compared with its photospheric value of 8.93 (Feldman 1992) both at the equator and mid-latitudes. This will be discussed further in Sect. 5. So far, absolute abundance for Fe and O have been determined at approximately 1.6 R$_\odot$, from the UVCS data. In order to obtain the abundances of other elements the DEM method,

described in Sect. 3, was used. This yields *relative* abundances and here were applied to both the UVCS and the CDS data.

In Fig. 7, plots of log DEM v. log T are presented for the UVCS data. The observed data points are superimposed, plotted with the values

$$\frac{I_{\mathrm{obs}}}{I_{\mathrm{th}}} \; DEM(T_{\mathrm{eff}}) \tag{11}$$

Table 5. Absolute abundances obtained from UVCS data, in "dex". The Fe abundance not labelled with the asterisk was derived from Eq. (7). The values labeled with the asterisc indicate the assumed photospheric value. The other elements abundances were found relative to Fe, from DEM.

Region	O	Mg	Al	Si	S	Ar	Ca	Fe
Photosphere	8.93	7.58	6.47	7.55	7.21	6.65	6.36	7.51
Equator Mar 1.58 $R_\odot$	8.15	-	-	7.25	-	6.30	-	7.51*
Equator Mar 1.6 $R_\odot$	8.00	7.10	6.00	7.25	-	6.30	-	7.51*
Midlat Mar 1.58 $R_\odot$	8.30	-	-	7.20	-	6.60	-	7.34
Midlat Mar 1.6 $R_\odot$	8.20	7.00	5.90	7.20	-	6.50	-	7.34
Midlat May 1.6 $R_\odot$	8.40	7.20	6.25	7.30	7.21	6.58	6.36	7.20

at the effective temperature of the line (T_{eff}). The effective temperature is defined as:

$$T_{\text{eff}} = \frac{\int T\, C(T)_{N_e}\, DEM(T)\, \mathrm{d}T}{\int C(T)_{N_e}\, DEM(T)\, \mathrm{d}T} \qquad (12)$$

where C(T), as said previously, is the contribution function for that line. This is a temperature average with respect to the DEM distribution and the contribution function.

To derive these curves the observed collisional components of hydrogen Lyα, Lyβ and O VI intensities have been used together with the other intensities. The Fe absolute abundance was already derived from log R v. log T plots (Sect. 4.1) for the March mid-latitude and May data. Using this value for the iron abundance in the DEM analysis resulted in good agreement with the H data points, confirming the validity of the log R v. log T method for the iron absolute abundance determination. So, the iron, together with the hydrogen, has been used as the reference element in the DEM analysis, for the rest of the elements. In this way there were more fixed data points and more constraints on the DEM evaluation were given. In the case of the March equatorial streamer, the log R v. log T method could not be applied. As already mentioned, iron was still used as the reference element together with the hydrogen in the DEM analysis, but assuming a photospheric abundance. However, comparing the iron and hydrogen points on the DEM plot, it seems that this assumption was a good approximation (see Fig. 7). Similarly, the iron lines at $1.6R_\odot$ in the mid-latitude March data were not strong enough to determine the absolute abundances from the log R v. log T plots. For this reason the DEMs at $1.6R_\odot$ have been calculated assuming the iron abundance to be that derived for $1.58R_\odot$. It should also be noted that in the following analysis the Fe XII line has not been used to constrain the fit because, compared to the other iron lines in the spectra, it appeared to be inconsistent. While for all the other iron ions, the ratio between the theoretical intensity and the observed intensity remains within a factor 2, for Fe XII it can reach 3.6 (for one of the equatorial regions).

This problem is well known, and it can be partly attributed to the atomic physics (Landi & Landini 1998). Another possibility is an uncertainty in the sensitivities of the detector here, because of considerable 'burn-in' at the location of this line.

The derived abundances, in logarithmic form, are listed in Table 5, while Table 6 shows the ratios of the derived abundances to photospheric values. To give an estimate of the errors

Table 6. $A_X(obs)/A_X(phot)$ for UVCS data

Region	O	Mg	Al	Si	Ar	Fe
Equator Mar 1.58 $R_\odot$	0.17	-	-	0.50	0.45	1.00
Equator Mar 1.6 $R_\odot$	0.12	0.33	0.34	0.50	0.71	1.00
Midlat Mar 1.58 $R_\odot$	0.23	-	-	0.45	0.89	0.68
Midlat Mar 1.6 $R_\odot$	0.17	0.26	0.27	0.45	0.71	0.68
Midlat May 1.6 $R_\odot$	0.29	0.42	0.60	0.56	0.85	0.48

Table 7. Element abundances from UVCS data, obtained relative to the Fe photospheric abundance (specified in "dex"). This analysis is provide for comparison with the CDS results given in Table 8

Region	O	Mg	Al	Si	Ar	Ca	Fe
Midlat Mar 1.58 $R_\odot$	8.40	-	-	7.30	6.65	-	7.51
Midlat Mar 1.6 $R_\odot$	8.30	7.10	6.00	7.20	6.50	-	7.51

in the abundance evaluation, we calculated the largest change in abundances which is still compatible with the observed line intensities, assumed to be subject to a 20% error. This results in a logarithmic error for the abundance of the order of ± 0.05.

In concluding this part we point out that the DEM analysis, as an independent method from that given in Eq. (9) and (10), confirms the oxygen depletion, with respect to its photospheric abundance, also found from the collisional and radiative oxygen components (see Table 4). We now move on to the analysis of abundances from CDS data: this will allow us to see if there is a variation in abundance with altitude. However, to facilitate this comparison, we give, in Table 7, *relative* abundances, still derived from the DEM technique, but assuming Fe to have its photospheric abundance. This is because no hydrogen line being present in CDS spectra, only *relative* abundances can be derived. The table lists only values for the mid-latitude streamers as the equatorial streamer abundance relative to photospheric iron is already listed in Table 5. Changes in the values given in Table 7 may be considered an indication of the uncertainties arising from errors in the determination of the absolute abundance of the iron.

As previously mentioned, CDS spectra include lines from ions which form over a wide range of temperatures. Iron, in particular, is present in a large number of ions, and this motivates our choice of iron as a reference element for the DEM technique. However, most of the lines in both the equatorial and

the mid-latitude spectra, originate from high temperature ions: no Fe lines, for $\log T \leq 5.95$, appear in the CDS data. The "coolest" lines are emitted by O III, O IV, O V, Ne VI and, at times, Ne VII ions (temperature of formation, $\log T$= 5, 5.2, 5.22, 5.61, 5.71, respectively). With no overlap with the elements that have high temperature lines, the DEM curves are not well constrained at the low temperature. For this reason, the O and Ne abundances are not obtained. We tried to overcome this problem, by assuming photospheric abundances for oxygen and neon (8.93 and 8.11, respectively), if we rely on UVCS streamer results, the oxygen abundance should be either lower or equal to the photospheric one. Moreover, coronal abundances found in the literature (Meyer 1985) are lower than photospheric abundances, both for O (8.39) and Ne (7.54). With this assumption, we found lower limits to the log DEM v. log T curve at low temperatures. If the abundance is given, in the theoretical line calculation only the DEM is unknown. It is found by minimizing the discrepancy between the theoretical intensity value and the observed intensity. In this case, the minimum value for the DEM at the temperature of the data point, is derived via the relation between element abundance and DEM (see Eq. (2)), with the assumption of photospheric abundances.

Fig. 8 (top and bottom panels) shows the log DEM v. log T curves for, respectively, the equatorial and the mid-latitude, data. As discussed above, *relative* abundances have been estimated, with Fe as a reference element.

Abundances for both streamers are given in Table 8 and, apart from Mg and perhaps S, do not significantly differ from photospheric abundances (shown in Table 5). Scarcely any FIP effect shows up in CDS data, with respect to photospheric element abundances. Sulphur is the only case where a depletion, with respect to the photospheric value, is found. This element has a FIP of 10.36 eV, thus its behavior is not clearly recognizable as belonging either to high or low FIP elements. Raymond et al. (1998) found it to behave like a high FIP element, while Feldman et al. described its behaviour as an intermediate case.

A comparison of UVCS abundances with CDS abundances shows a decrease with height for all elements (Ca is an exception, but this line appears only in one UVCS spectrum) in the altitude interval between the regions observed by the two instruments.

5. Conclusions

In this section we discuss the results we obtained from different techniques and compare the present results with those found by other authors. Issues which, in our opinion, deserve further work, are also pointed out. We organize this session by physical parameters, dealing sequentially with temperatures, densities and abundances.

5.1. Electron temperatures

Using coordinated CDS and UVCS observations, profiles of electron temperatures v. solar distance were derived for an equatorial and a mid-latitude streamer, over the range from $1.02\ R_\odot$

Table 8. Element abundances obtained from the CDS data, specified in "dex", relative to the abundance of Fe, assumed photospheric.

Region	O	Ne	Mg	Al	Si	S	Ca	Fe
Equator Mar	8.93	8.11	7.4	6.47	7.55	-	6.3	7.51
Midlat Mar	8.93	8.11	7.5	6.47	7.5	7.1	6.36	7.51

to 1.19 $R_\odot$ from CDS data and at $1.58 - 1.6 R_\odot$ from UVCS data. CDS results show an electron temperature increasing with distance, up to the highest altitude reached by the data. This behaviour is consistent with results found for streamers' temperatures, during the Whole Sun Month campaign, by Gibson et al. (1999a), from radial power law fits to densities, and for equatorial regions, during the same campaign, by Fludra et al. (1999), from the line ratio technique. These authors used ratios of lines from different elements, hence introducing possible uncertainties related to uncertainties in element abundances. Here we avoided this problem by using ratios of lines from different ionization stages of Fe. Gibson et al. temperatures are obviously not electron temperatures, although apparently streamer conditions are such that electron scale-height and proton temperatures (Raymond et al. 1998) are about equal. UVCS temperatures turn out to be consistent with previous determinations ($\log T$= 6.13-6.2 K) at approximately the same altitude (Raymond et al. 1998, 1997). When UVCS electron temperature results are considered, in conjunction with simultaneous values obtained from CDS data, we extend our knowledge of the electron temperature v. height profile, inferring that the electron temperature reaches a peak at altitudes in between 1.19 and 1.6 $R_\odot$. Differences between electron temperatures in the three streamers we analyzed are minor, with the mid-latitude streamers showing higher values, particularly at the lower levels. These results together with the presence of the loop-system at the base of the March mid-latitude streamer, can give an indication of the presence of an "active" streamer, for the mid-latitude case, and a "quiet" streamer, for the equatorial case. Hence, streamer temperatures can range between 1.1 and 1.5 10^6K, in the altitude range we analyzed. These temperatures are somewhat higher than coronal hole temperatures (see, e.g. Fludra et al. 1999; David et al. 1998) and point to different mechanisms of heating deposition. The temperature profiles of Fig. 3 may be used to put constraints on the *ad hoc* heating functions often used when modelling different coronal structures (see, e.g. Wang et al. 1998, Suess et al. 1999). A high priority for future observations will be to fill the gap between 1.19 and 1.5-1.6 solar radii and locate where the electron temperature reaches a maximum, thus providing further indications on the heating mechanism v. altitude behavior.

At distances of the order of 1.5–1.6 $R_\odot$ streamers are usually said to be isothermal (see e.g. Raymond et al. 1997; Feldman et al. 1998). It is interesting to note that both the convergence of the profiles from different ratios in Fig. 3 (upper) and the DEM curves from CDS spectra show the plasma to be isothermal also at lower altitudes (the second peak in the March mid-latitude data is likely to be due to the hot loop system present in the CDS field of view). Although our March structures are more or less
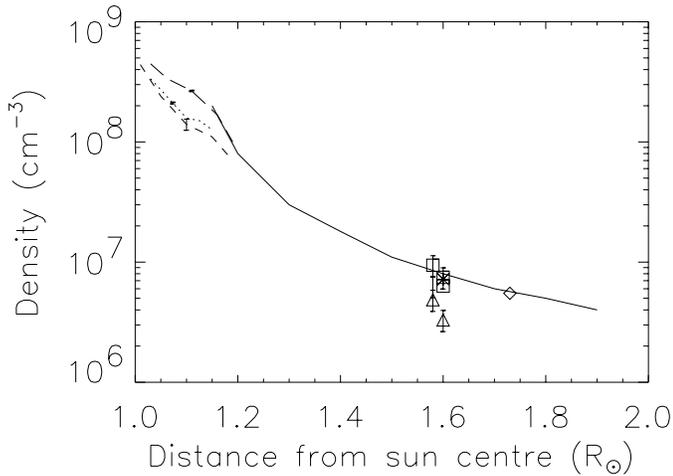
Fig. 9. Streamer density v. solar distance for the present work compared to previous studies. Square are mid-latitude, and triangle are equatorial UVCS data; the long dashed and dotted curves are from CDS Si IX ratios from, respectively, the mid-latitude and the equator. Solid line is density from Gibson et al. (1999a); dashed line is from Fludra et al. (1999); diamond from Strachan et al. (2000); asterisk from Ciaravella et al. (1999).

consistent with this claim, the May streamer shows evidence for a multi-temperature plasma, both from the DEM analysis and from the Fe $\log R$ v. $\log T$ curves. Extended observations would be needed to understand whether this is a property of active v. stable structures, or whether it is linked to a special time in the streamer's life. On the other hand, the presence of lines from low temperature plasma may possibly originate from cooler material in the fore/background – EIT images show the streamer to be close to a coronal hole structure – which, however, could not affect the high temperature section of the DEM curve.

5.2. Densities

Streamers' densities have been known for some time, because they can be derived from polarized brightness (pB) measurements. However, pB values usually refer to levels ≥ 1.1 solar radii. The line ratio technique can provide values at lower heliocentric distances. Doschek et al. (1997) derived off-limb density for coronal hole and quiet sun, using Si VIII and S X line ratios for distance very close to the solar limb. Their results in the quiet region give densities of about 6-7 $\times 10^7$ cm^{-3} for a distance of 1.15 R$_\odot$, somewhat lower than the present results. In a later study, Doschek et al. (1998a) used Si VIII line ratio to derive a density profile, for an equatorial streamer. This profile shows a trend similar to ours, but still with lower values compared to our ones. In Fig. 9 we show some recent determinations of streamer densities, along with the results presented here. The streamer densities from Gibson et al. (1999a) refer to a streamer observed only a few months after we made our observations. Gibson et al. Fig. 9 shows how the pB derived densities are consistent with the densities derived from line ratios at low distances, yielding a less steep profile of N_e v. solar distance

than it would be extrapolated from white light measurements only. Our results from both streamers confirm this trend.

Density measurements from UVCS data by Strachan et al. (2000) and Ciaravella et al. (1999) are also shown in the figure, together with another CDS study (Fludra et al. 1999). However, we point out that our streamers do not show evidence of the weak O VI emission core sometimes appearing in UVCS streamers, hence present densities have been compared with values given for the streamers "legs" by previous authors. Densities from UVCS measurements may vary both because of a real density variation from streamer to streamer as well as because of the lack of simultaneous measurements of disk intensities, which are needed for a correct usage of the relationship (see Sect. 4.2, Eq. (8)) from which densities have been derived. The influence of this factor is hardly quantifiable, as we do not really know how large a variation we can expect in the O VI 1032 disk intensities.

We also point out that the March and May mid-latitude streamers appear to have higher densities than the equatorial March streamer. Although in the low corona the March structure may be affected by the presence of the hot loop, the UVCS determination, yielding a higher density as well, supports CDS results. It will be up to future observations to find out whether this is an occasional episode or whether mid-latitude or active streamers do have higher densities than quiet structures. Also, the density variation across streamers still needs to be investigated.

5.3. Composition

In this work, the absolute oxygen abundance at $1.58 - 1.6$ R$_\odot$ has been derived by using two different methods: both agree in revealing an oxygen depletion, with respect to the O photospheric abundance ($\log A_O = 8.93$), that can be as much as $\approx 80\%$ at the equator (see Table 5). Even if in our streamers it is not possible to identify the core and the legs as in Raymond et al. (1997, 1998), our results match the oxygen abundances found by these authors at 1.5 R$_\odot$ and 1.75 R$_\odot$. There are a few estimates of the oxygen streamer abundance in the literature: in the Raymond et al. work, the oxygen abundance was found to vary, in the streamer core, from 7.5 to 7.8 and in the streamer's legs – or, when core/legs cannot be identified, in the overall structure – 8.3 to 8.66, while in Ciaravella et al. (1999) a value of ≈ 8.8 is given for the O streamer abundance, and a value of only 8.1 in a related transient event. These values point to a large variation in O abundance, both within streamers and in different structures.

At lower altitudes, the oxygen abundance is hardly known and it is unfortunate that no value can be derived from our CDS data. From SUMER observations, Feldman et al. found (at heights ≤ 1.03 R$_\odot$) an oxygen abundance of 8.8, in equatorial regions. We do not know, from this single measurement, whether the O abundance decreases with altitude, or whether the Feldman measurement refers to a streamer not showing oxygen depletion.

In the solar wind, there are a few abundance determination for oxygen. Wimmer Schweingruber (1994) gives 8.72 in slow

wind and 8.8 in high speed wind: hence the depletion of oxygen in the solar wind is too marginal to be convincing. On the other hand, recent work by Aellig et al. (1999) finds an Fe/O ratio which changes as a function of the solar wind speed. Their flux weighted average for the Fe/O ratio is 0.11 ± 0.03 and it is consistent with the average Fe/O ratio we derive from UVCS abundances of 0.13. In deriving this value, an average of the oxygen values from Table 4 were used. A slightly higher value is obtained if values from Table 5 are used, but it should be remembered that in this case only the collisional component of the oxygen lines was used. These values are also consistent with the in-ecliptic solar wind value given by Ipavich et al. (1991): it might be interesting to check on Fe/O variation along/across streamers, in order to get more insight about the slow wind origin.

For the other elements, at $1.58 - 1.6\ R_\odot$ all abundances show a depletion, with respect to their photospheric values, in agreement with Raymond at al. (1997) results. Although spectra at different altitudes are slightly different, not always allowing multiple determinations of the abundance of the same element, the results we got are fairly consistent with each other.

The scarcity of high FIP elements in our UVCS and CDS spectra does not allow us to analyze the FIP effect (e.g. Young & Mason 1997; Doschek et al. 1998b; Laming et al. 1999) either at low heliocentric distances or at about 1.6 R$_\odot$. However, streamers are known to behave anomalously, as far as the FIP effect is concerned: Schmelz (1999) pointed out that contrasting results, in this field, have been obtained by Feldman et al. (1998) and Raymond et al. (1997). Present UVCS results support Raymond's findings that low FIP elements are depleted, with respect to their photospheric abundances, but we have puzzling results for the (only) two high FIP elements in our spectra. Raymond et al. (1997) find high FIP element depletion to be about a factor 2 larger, e.g. for O, Ar, S, than for low FIP elements, like Si, Fe, Al. Here we find oxygen to be more depleted than low FIP elements, but Ar is consistently found to be less depleted than low FIP elements. It is difficult to explain this behaviour, but we notice that it is not unusual to find some inconsistency in the "behaviour" of high FIP elements. For instance, in the Aug 21 streamer analyzed by Raymond et al. (1998), an O enhancement, with respect to coronal abundances, by about a factor 2, corresponds to a S depletion of about a factor 3.5 (still with respect to coronal abundances). The dependence of the FIP effect on the streamer type (whether it is a stable, quiescent structure, or an active phenomenon, to which fresh photospheric material can occasionally contribute) and, possibly, on the streamer lifetime is still a poorly known issue, which deserves further study.

References

Aellig M.R., Hefti S., Grunwaldt H., et al., 1999, JGR 104, 24769
Brosius J.W., Davila J.M., Thomas R.J., et al., 1996, ApJS 106, 143
Callaway J., 1994, Atomic Data Nucl. Data Tables 57, 9
Ciaravella A., Raymond J.C., Strachan L., et al., 1999, ApJ 510, 1053
David C., Gabriel A.H., Bely-Dubau F., et al., 1998, A&A 336, L90
Del Zanna G., 1999, Ph.D. Thesis, Univ. of Central Lancashire
Del Zanna G., Bromage B.J.I., 1999a, Space Sci. Rev. 87, 169
Del Zanna G., Bromage B.J.I., 1999b, JGR 104, 9753
Dere K.P., Landi E., Mason H.E., et al., 1997, A&AS 125, 149
Doschek G.A., Warren H.P., Laming J.M., et al., 1997, ApJ 482, L109
Doschek G.A., Banerjiee D., Perez M.E., 1998a, Solar Phys. 181, 91
Doschek G.A., Laming J.M., Feldman U., et al., 1998b, ApJ 504, 573
Feldman U., 1992, Phys. Scripta 46, 202
Feldman U., Schuhle U., Widing K.G., et al., 1998, ApJ 505, 999
Fludra A., Del Zanna G., Alexander D., et al., 1999, JGR 104, 9709
Gabriel A.H., Garton W.R.S., Goldberg L., et al., 1977, ApJ 169, 595
Gardner L.D., Kohl J.L., Noci G., et al., 1996, BAAS 188, 37.05
Gibson S.E., Fludra A., Bagenal F., et al., 1999a, JGR 104, 9691
Gibson S.E., Biesecker D., Guhathakurtha M., et al., 1999b, ApJ 520, 871
Harrison R.A., Sawyer E.C., Carter M.K., et al., 1995, Solar Phys. 162, 233
Haugan S.V.H., 1997, CDS software note No. 47
Hummer D.G., 1994, MNRAS 268, 109
Hummer D.G., Storey P.J., 1987, MNRAS 224, 801
Ipavich F.M., Galvin A.B., Geiss J., et al., 1991, In: Solar Wind Seven. Proceedings of the 3rd COSPAR Colloquium, Goslar, Germany, p. 239
Kohl J.L., Esser R., Gardner L.D., et al., 1995, Solar Phys. 162, 313
Laming J.M., Feldman U., Drake J.J., et al., 1999, ApJ 518, 926
Landi E., Landini M., 1998, A&A 340, 265
Li J., Raymond J.C., Acton L.W., et al., 1998, ApJ 506, 431
Mason H.E., Monsignori Fossi B.C., 1994, A&AR 6, 123
Mazzotta P., Mazzinelli G., Colafrancesco S., et al., 1998, A&AS 133, 403
Meyer J.-P., 1985, ApJS 57, 173
Noci G., Kohl J.L., Withbroe G.L., 1987, ApJ 315, 706
Noci G., Kohl J.L., Antonucci E., et al., 1997, In: Proc. V^{th} SOHO Workshop, ESA-SP 404, p. 75
Raymond J.C., Kohl J.L., Noci G., et al., 1997, Solar Phys. 175
Raymond J.C., Suleiman R., Kohl J., et al., 1998, Space Sci. Rev. 85, 283
Schmelz J.T., 1999, In: Proc. 8th SOHO Workshop, ESA-SP 446, p. 585
Scholz T.T., Walters H.R.J. 1991, ApJ 380, 302
Strachan L., Panasyuk A.V., Dobrzycka D., et al., 2000, JGR 105, 2345
Suess S.T., Wang A.H., Wu S.T., Poletto G., McComas D.J., 1999, JGR 104, 4697
Vernazza J.E., Reeves E.M., 1978, ApJS 37, 485
Wang A.H., Wu S.T., Suess S.T., Poletto G., 1998, JGR 103, 1913
Wimmer Schweingruber R.F., 1994, Ph.D. Thesis, Univ. Bern
Withbroe G.L., 1978, ApJ 225, 641
Withbroe G.L., Kohl H.L., Weiser H, et al., 1982, Space Sci. Rev. 33, 17
Young P., Mason H.E., 1997, Solar Phys. 175, 523